Supplementary Materials for

Controllable bound states in the continuum enabling blue-to-green directional vortex lasing

Feifan Xu et al.

Corresponding authors: Zhe Zhuang, zzhuang@nju.edu.cn; Jun-long Kou, jlkou@nju.edu.cn; Yan-qing Lu, yqlu@nju.edu.cn; Bin Liu, bliu@nju.edu.cn

The PDF file includes:
Fig. S1 to S11
Text S1
Table. S1

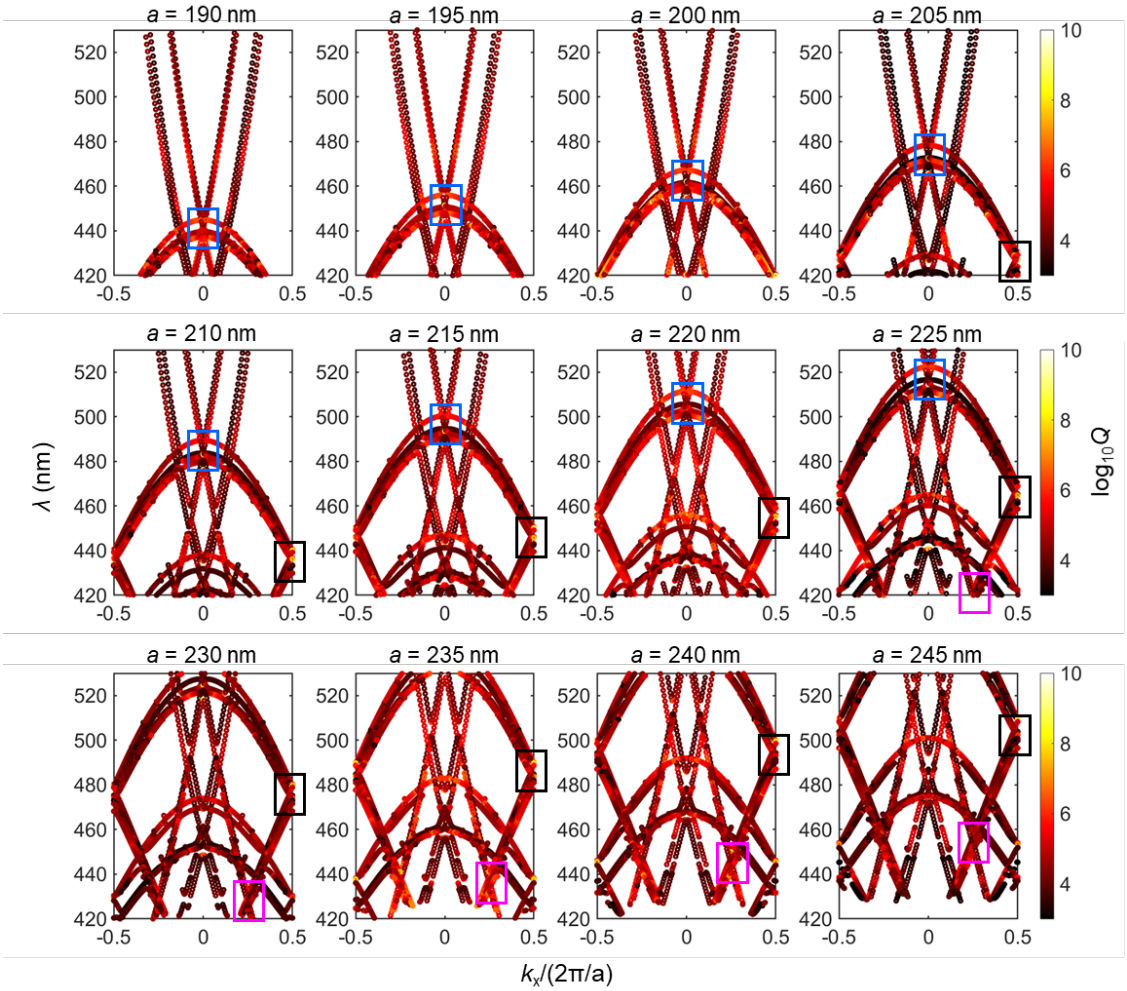

Fig. S1. Evolution of PhC bandstructures and Q-landscape versus lattice constant *a*. The calculated band diagrams and *Q*-factor maps for different *a* sweeping from 190 to 245 nm. The symmetry-protected on-Γ (blue rectangular boxes) and FW off-Γ BIC branches (k=0.25, purple boxes; k=0.5, black boxes) coexist in the hybrid cavity; this summarizes the k-space positions of high-*Q* spots relative to *a*, highlighting two practical control knobs for laser mode selection: tuning *a* or adjusting the gain spectrum to overlap the desired open *Q*-channel.

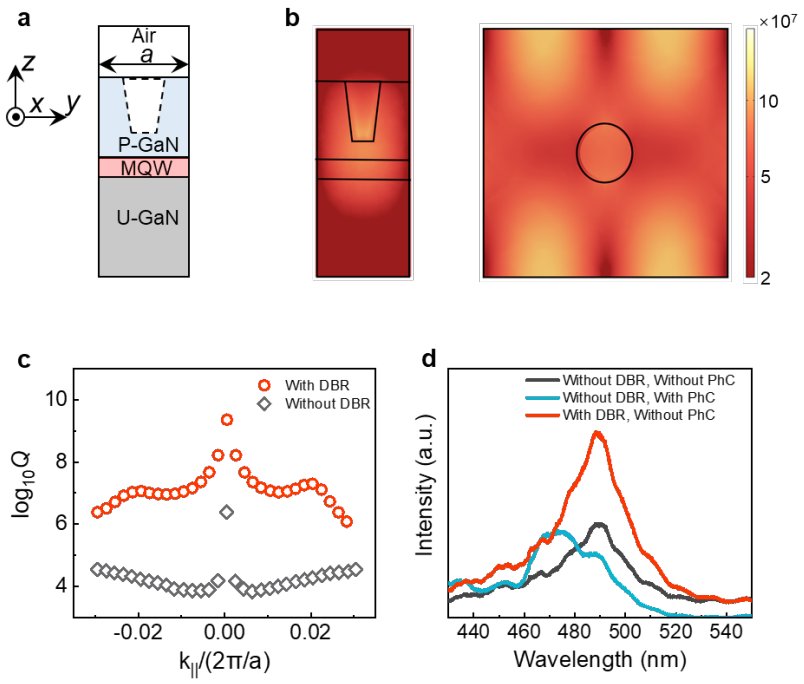

Fig. S2. Impact of the DBR on field confinement and *Q*. a, b, Vertical stack and simulated longitudinal field profiles ($|E|^2$) without the porous-GaN/GaN DBR, showing a field that is much lower than that of the hybrid-cavity structure. c, *Q* factors near Γ reveal an enhancement of the radiation-limited quality factor by ~3 orders of magnitude when the DBR is included. d, The PL spectra of samples without DBR and PhC, without DBR but with PhC, and without PhC but with DBR at a pumping density of 2 mJ/cm^2, which was below the thresholds for all samples. These results evidence stronger vertical feedback and improved lateral coupling in the hybrid cavity.

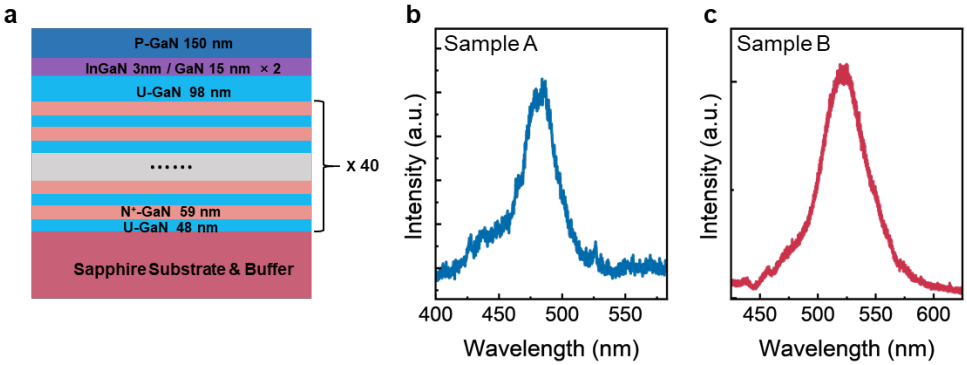

Fig. S3. Epitaxial structures and gain spectra. a, Schematic of the epilayer stacks for Samples A and B. Only indium composition in MQWs differed between Samples A and B. b, Room-temperature photoluminescence (PL) with peaks at 478 nm (Sample A) and 523 nm (Sample B).

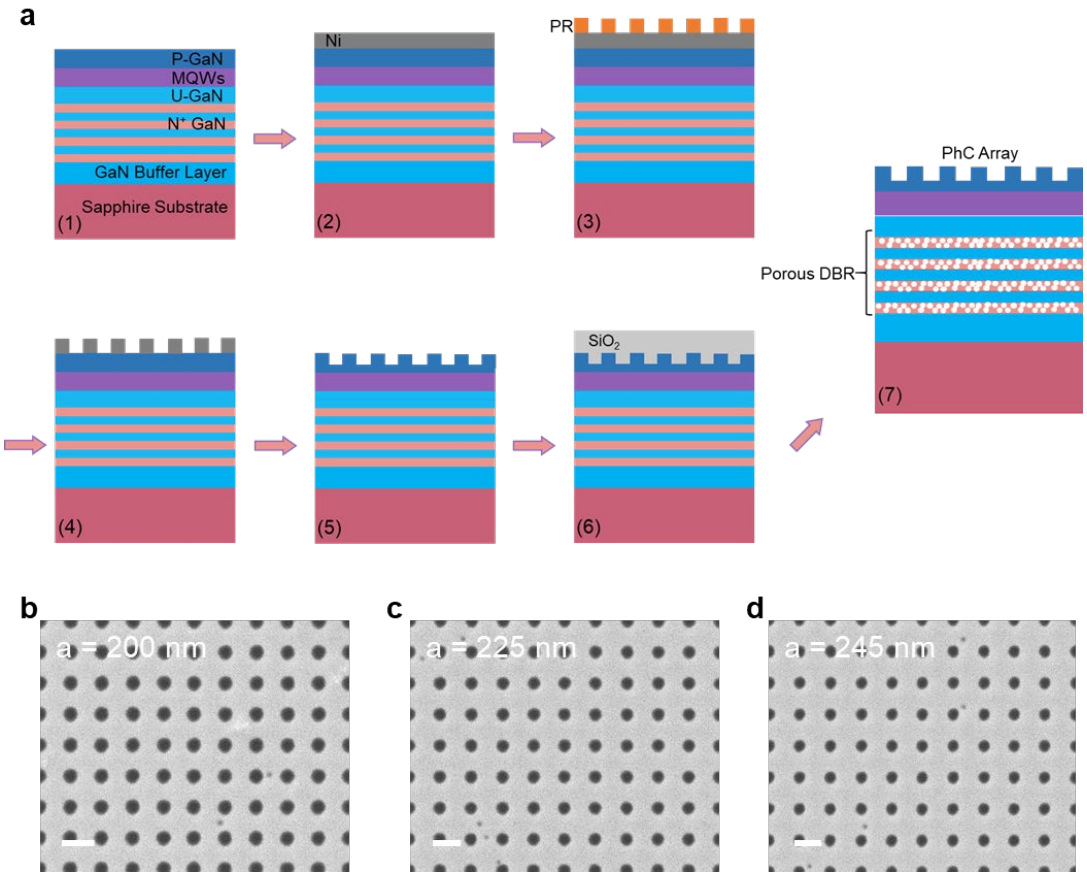

Fig. S4. Fabrication flow for the hybrid-cavity GaN BIC laser. a, Process sequence: Ni hard-mask deposition; electron-beam lithography (EBL); Ar-plasma removal of exposed Ni; Cl_2/BCl_3 ICP etch to form GaN nanoholes; SiO_2 protection bar patterning; selective electrochemical porosification of heavily doped GaN layers to form the porous-GaN/GaN DBR; removal of the protection layer. b-d, Top-view SEM images of the device with a = 200 nm, 225 nm, and 245 nm. (scale bar: 200 nm)

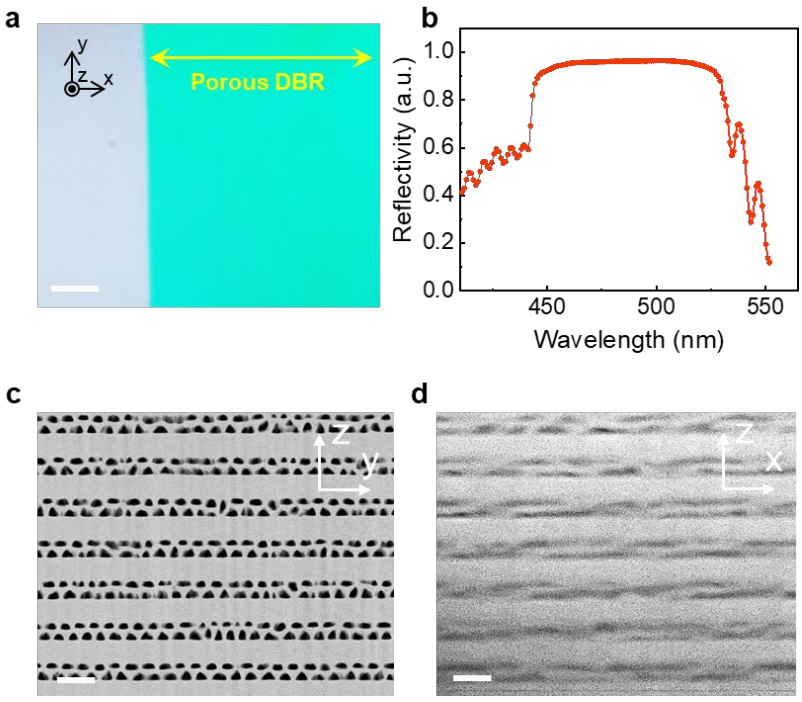

Fig. S5. Porous-GaN/GaN DBR optical response and anisotropy. a, Image of the sample after electrochemical porosification, the green area represents DBR, (scale bar: 50 μm). b, Normal-incidence reflectivity spectrum, showing >96.5% peak reflectivity and a stopband ≈ 70 nm. c, d, SEM images of the DBR in y-z and x-z cross-sectional views, revealing pore-shape anisotropy. (scale bar: 100 nm)

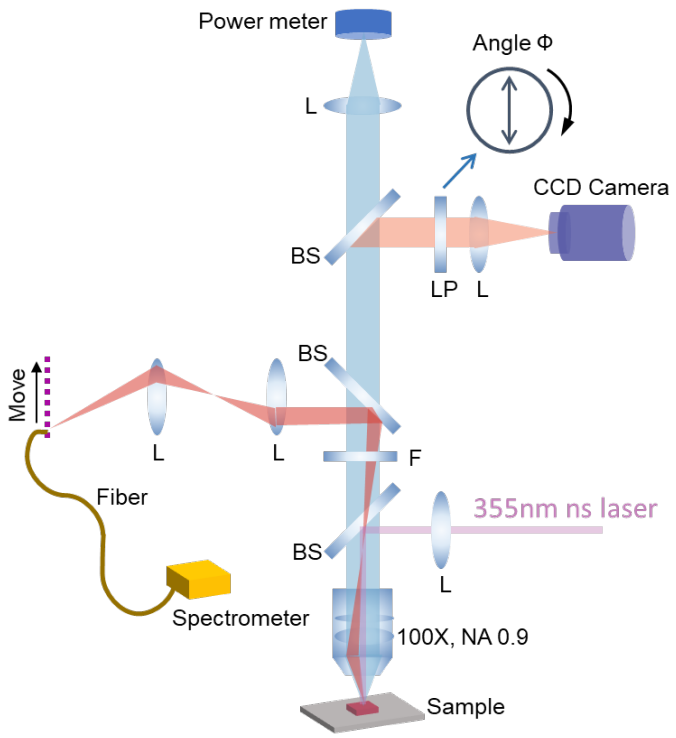

Fig. S6. Optical characterization setup. Schematic of the customized microscope platform enabling angle-resolved spectroscopy, far-field imaging, polarization analysis and power readout: a 355-nm nanosecond laser is focused through a 100×, 0.90 NA objective; emission is relayed to the Fourier plane where a scanning fiber probe feeds a grating spectrometer to build k–λ maps; a camera records Fourier-plane images; a rotatable linear polarizer provides polarization-resolved far-fields; a power meter records the emitted power.

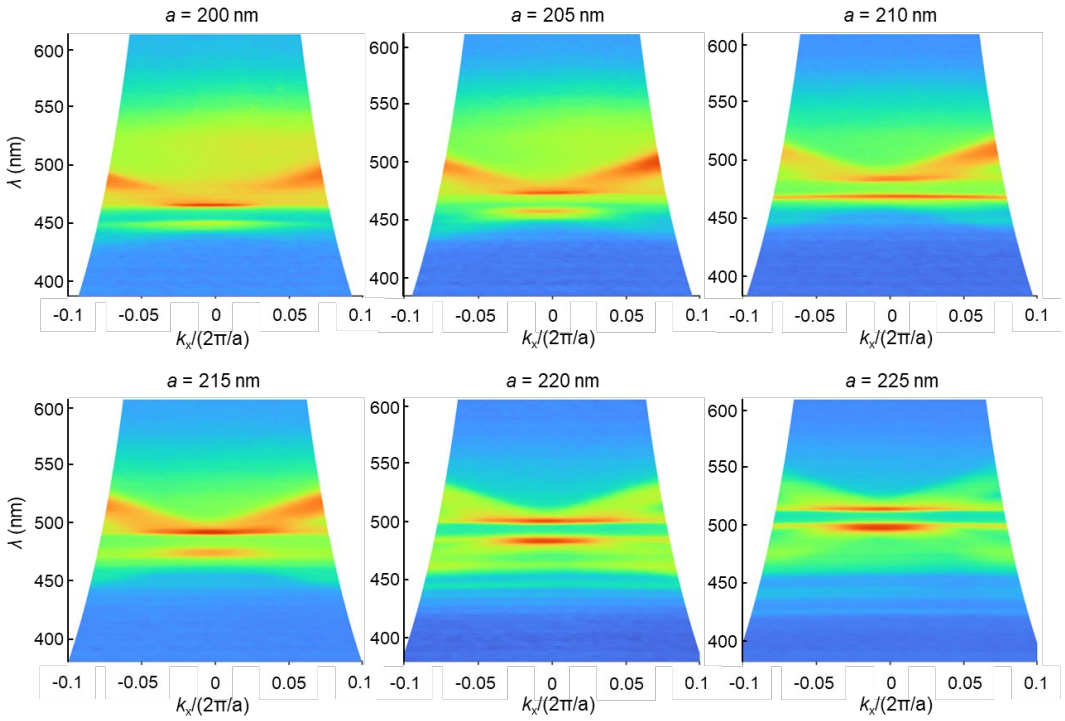

Fig. S7. Sub-threshold band structures confirming a quasi-flat band near Γ. Angle-resolved k–λ maps for on-Γ lasers with a = 200-225 nm under sub-threshold pumping. A quasi-flat feature at the laser wavelength remains nearly dispersionless near Γ, consistent with the designed low-group-velocity band that supports low thresholds.

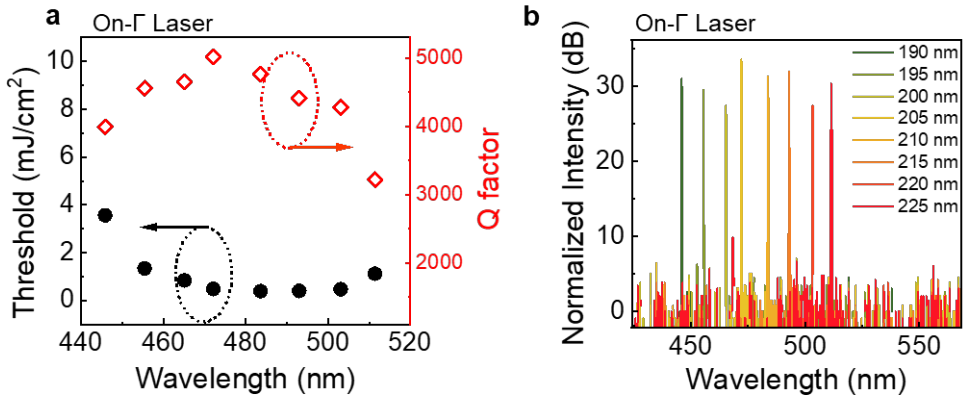

Fig. S8. Thresholds, *Q* factor and SMSR for on-Γ BIC lasers across lattice constant. a, Threshold and Q factor versus lasing wavelength (a = 190–225 nm) for Sample B. b, PL spectrum of the on-Γ lasers with lasing wavelengths tuning from 445.8 nm to 511.4 nm without mode hopping. SMSR exceeds 20 dB for all lasers and reaches up to 28.4 dB.

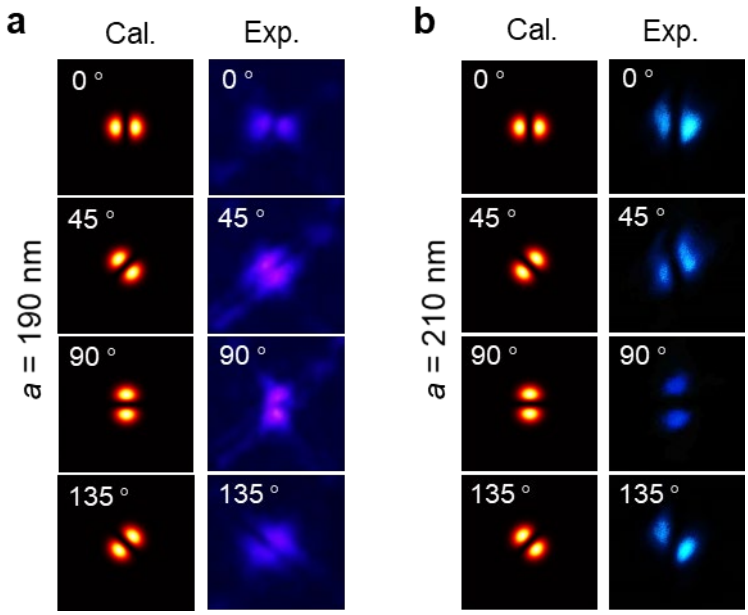

Fig. S9. Reproducible switching of vortex topological charge. a, Simulated and measured polarized far-field patterns for a =190 nm, showing topological charge +1. b, Simulated and measured polarized far-field patterns for a = 210 nm, showing topological charge -1. The opposite signs confirm lattice-controlled switching of the polarization-vortex topological charge.

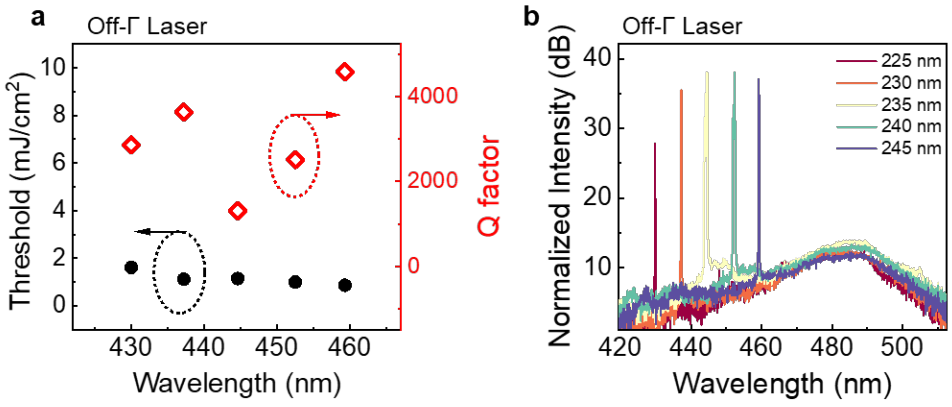

Fig. S10. Thresholds, *Q* factor and SMSR for off-Γ BIC lasers across lattice period. a, Threshold and Q factor versus lasing wavelength (a = 225-245 nm) for Sample A. b, PL spectrum of the off-Γ lasers with lasing wavelengths tuning from 430 nm to 460 nm without mode hopping. SMSR exceeds 15 dB for all lasers and reaches up to 25 dB.

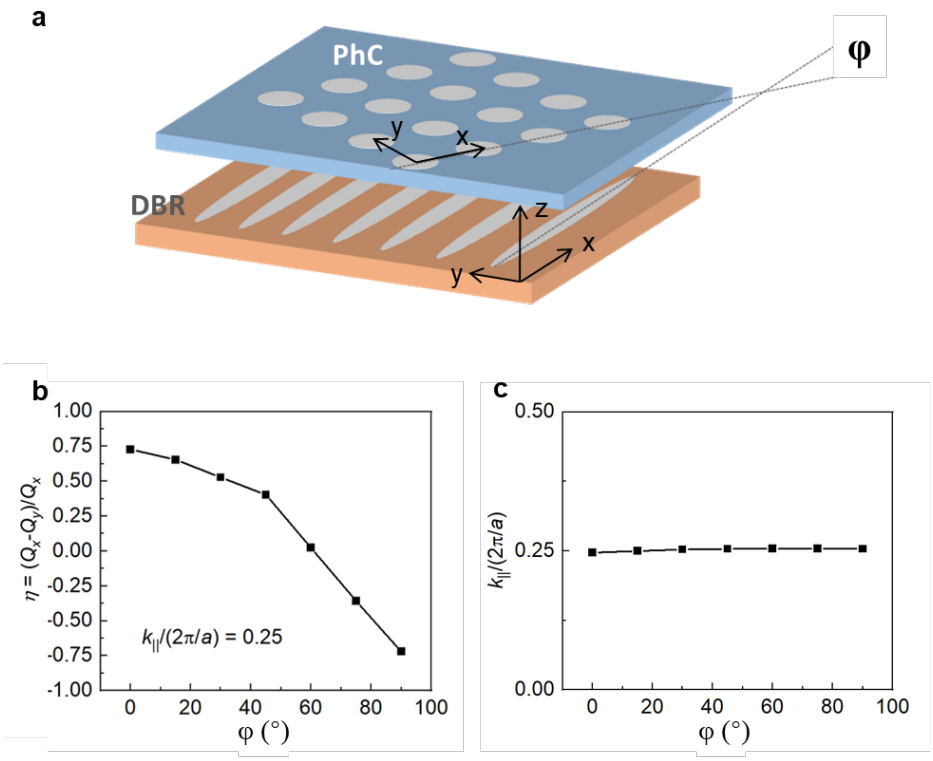

Fig. S11. Effect of DBR anisotropy and twist angle on mode selection. a, Simplified schematic of the simulation geometry. The twist angle φ is defined as the angle between the lattice axis x of the PhC and the primary etch direction (x-axis) of the porous DBR. All other structural parameters remain constant, with a fixed in-plane refractive index difference of $\Delta n = 0.28$ within the DBR. b, Simulated evolution of the Q factors for the orthogonal off-Γ modes as a function of φ. At $\varphi = 0°$, the refractive index anisotropy breaks the competition equilibrium between orthogonal modes, suppressing the Q of the y-oriented mode by 75% and granting a decisive advantage to the x-oriented mode (corroborated by the x-axis far-field emission pattern). As φ increases, the difference in Q factors decreases, can restore C_{4v} emission characteristics near $\varphi = 60°$. A further increase in φ eventually switches the system to a y-axis dominant emission channel. c, Momentum-space stability. The magnitude of the wavevector (k-position) for the off-Γ mode remains invariant with respect to the twist angle φ.

Text S1: The BIC locking at a fixed location in normalized momentum space.

Considering two adjacent leaky modes in a photonic crystal slab (for example, a pair of dipole and quadrupole resonances), their dynamics can be described by coupled-mode theory:

$$\frac{d}{dt}\begin{pmatrix} a_1(t) \\ a_2(t) \end{pmatrix} = [i\mathbf{\Omega}(k) - \mathbf{\Gamma}]\begin{pmatrix} a_1(t) \\ a_2(t) \end{pmatrix}$$

where $a_{1,2}(t)$ are the complex amplitudes of the modes. The frequency and loss matrices of the system are respectively:

$$\mathbf{\Omega}(k) = \begin{pmatrix} \omega_1(\mathbf{k}) & \kappa \\ \kappa^* & \omega_2(k) \end{pmatrix}, \mathbf{\Gamma} = \begin{pmatrix} \gamma_1 & 0 \\ 0 & \gamma_2 \end{pmatrix}$$

Here, $\omega_{1,2}(k)$ are the eigenfrequencies depending on the in-plane momentum k, $\gamma_{1,2}$ are the radiation loss rates of the modes, and κ is the coupling coefficient between the modes.

Diagonalizing the system matrix yields two eigenfrequencies:

$$\omega_{\pm}(k) = \bar{\omega}(k) \pm \sqrt{\Delta\omega(k)^2 + |\ \kappa\ |^2} - i\bar{\gamma}$$

with $\bar{\omega}(k) = \frac{\omega_1(k)+\omega_2(k)}{2}$, $\Delta\omega(k) = \frac{\omega_1(k)-\omega_2(k)}{2}$, and $\bar{\gamma} = \frac{\gamma_1+\gamma_2}{2}$.

A FW BIC emerges at a particular in-plane wavevector k_{BIC}. The following two requirements are simultaneously satisfied:

1. **Frequency degeneracy**: $\omega_1(k_{BIC}) = \omega_2(k_{BIC})$, i.e., $\Delta\omega(k_{BIC}) = 0$.
2. **Destructive radiation interference**: The radiation channels of the two modes interfere completely and coherently, resulting in zero total radiation loss for one of the eigenstates. Mathematically, this requires the coupling coefficient κ to be real and the loss rates to satisfy $\gamma_1 = \gamma_2 = \gamma$.

In conventional photonic crystal slabs, the radiation loss rates $\gamma_{1,2}$ of the modes strongly depend on the vertical boundary conditions. For a mode whose original downward radiation loss rate is $\gamma_{\perp}^{0}$, the effective vertical loss is modified to:

$$\gamma_{\perp}^{\text{eff}} = \gamma_{\perp}^{0} \cdot [1 - R \cdot \exp(i2\beta d)]$$

where β is the propagation constant in the vertical direction and d is the separation between the DBR and the photonic crystal slab. In this work, the introduction of a high-reflectivity porous DBR at the bottom serves the key function of almost completely suppressing the downward radiation channel. Assume that the reflectivity of the DBR in the target spectral band is $R \approx 1$. When phase matching is satisfied, $R \to 1$, $\gamma_{\perp}^{\text{eff}} \to 0$.

Consequently, in the hybrid cavity, the total radiation loss of the modes is dominated almost entirely by in-plane leakage processes:

$$\gamma_{1,2} \approx \gamma_{\parallel,1,2}^{\text{PhC}}$$

The vertical feedback provided by the DBR remains efficient and stable over the entire broad tuning range (e.g., 66 nm; $\partial R / \partial \lambda \approx 0$). This renders the vertical loss term a negligible constant background in the Friedrich-Wintgen condition. Whether a BIC forms and how stable it becomes are therefore determined solely by the in-plane

processes, which can be precisely engineered through the photonic crystal band structure.

Photonic crystal bands possess an intrinsic scaling property. For fixed dimensionless geometric parameters (normalized thickness t/a), the dimensionless dispersion relation is given by:

$$\widetilde{\omega}(u) = \frac{a}{2\pi c}\omega(k)$$

$\widetilde{\omega}(u)$ represents the momentum space position of the FW BIC that achieves perfect destructive interference, where $u = a \mid k \mid$ is the dimensionless momentum and c is the speed of light. Changing the absolute lattice constant a is equivalent to linearly scaling the band along the frequency axis:

$$\omega(k; a) = \frac{2\pi c}{a} \cdot \widetilde{\omega}(u)$$

Therefore, the frequency degeneracy condition $\omega_1(k; a) = \omega_2(k; a)$ that determines the BIC location translates into finding a fixed point u_{BIC} in the dimensionless momentum space:

$$\widetilde{\omega}_1(u_{BIC}) = \widetilde{\omega}_2(u_{BIC})$$

This solution u_{BIC} depends solely on the dimensionless geometry of the photonic crystal and is independent of the absolute period a. Consequently, the actual momentum position of the BIC is:

$$\mid k_{BIC}(a) \mid = \frac{u_{BIC}}{a}$$

The far-field emission angle θ of the laser is determined by the in-plane momentum, $sin\ \theta \approx \mid \boldsymbol{k}_{BIC} \mid \lambda/(2\pi n_{eff})$. Substituting the above relation yields:

$$\theta(a) \approx arcsin\left[\frac{\lambda}{2\pi n_{eff}} \cdot \frac{u_{BIC}}{a}\right]$$

In experimental tuning, the resonance wavelength λ_{BIC} of the BIC is approximately proportional to a ($\lambda_{BIC} \propto a$). Hence, the ratio λ_{BIC}/a remains nearly constant throughout the tuning process, resulting in a stable emission angle θ. This theoretically explains why the off-Γ emission maintains angle locking across the *a* tuning range.

Table S1. Survey of published BIC lasers: BIC type, gain medium, emission wavelength, threshold, *Q* factor, wavelength-tuning range, and SMSR.

Type	Gain medium	Wavelength (nm)	Threshold	*Q*	Δλ/λ (%)	SMSR (dB)	Ref.
On-Γ BIC	GaAs/AlGaAs	3.15 THz	~0.19 kAcm^2	1440	/	25	(*26*)
On-Γ BIC	InGaAsP	1551	0.086 kW/cm^2	4700	4.2%	/	(*15*)
On-Γ BIC Off-Γ BIC	a-Sb_2Se_3 c-Sb_2Se_3	1545 1419	6.6 kW/cm^2 54.5 kW/cm^2	/	/	/	(*27*)
On-Γ BIC Off-Γ BIC	InAs/GaAs	1303/1328 1311	0.052 kW/cm^2 0.074 kW/cm^2	790 525	2.9%	/	(*28*)
On-Γ BIC	GaAs	1275	80 W/cm^2	32500	/	/	(*6*)
On-Γ BIC	GaAs	850 - 925	14 μJ/cm^2	2750	8.4%	/	(*29*)
On-Γ BIC	$CsPbBr_3$	782 - 789	4.28 mJ/cm^2	1100	0.9%	/	(*30*)
On-Γ BIC	CdSe/CdZnS	632 - 663	44.5 μJ/cm^2	2590	4.8%	/	(*19*)
Off-Γ BIC	$CH_3NH_3PbBr_3$	555	0.3 mJ/cm^2	1130	/	/	(*16*)
On-Γ BIC	GaN	367	55.46 kW/cm^2	2039	/	/	(*31*)
On-Γ BIC	GaN	371 - 380	16 mJ/cm^2	3700	2.4%	/	(*32*)
On-Γ BIC Off-Γ BIC	InGaN/GaN MQWs	445.5 - 511.5 429.7 - 459.2	0.39 mJ/cm^2 0.87 mJ/cm^2	5016 4593	13.8 % 6.7 %	28.4 25	This work